

Application of Gaussian-Beam Migration to Multiscale Imaging of the Lithosphere beneath the Hi-CLIMB Array in Tibet

by Robert L. Nowack, Wang-Ping Chen, and Tai-Lin Tseng*

Abstract In this study, we apply Gaussian-beam (GB) migration of scattered teleseismic *P* waves to image the crust and upper mantle beneath Tibet using data from the Hi-CLIMB experiment. We use teleseismic *P* waves from three groups of earthquakes to the southeast, northeast, and northwest of the Hi-CLIMB array, each within a narrow range of azimuth and distance, to obtain stacked radial receiver functions, which we then use to image the lithosphere by GB migration. We produced images at several different frequency bands in order to constrain the multiscale scattering properties of the lithosphere. For each frequency band, three GB images are generated, each from earthquake sources in a distinct back-azimuth group. The three images are then stacked to form a composite image. The imaged Moho is generally strong and continuous under much of the Lhasa terrane in southern Tibet, corresponding to a well-defined Moho. A major disrupted zone in Moho scattering, extending over 200 km in length, is evident in the vicinity of the Bangong–Nujiang suture, where there is also increased crustal scattering. The disrupted zone marks the diffuse, subsurface join between stable portions of mantle lithosphere under southern and central Tibet, respectively. At the northern end of the profile in the Qiangtang terrane there is an increase in Moho reflectivity but at a shallower depth than under the Lhasa terrane. Comparable length scales of about 200 km between regions with disrupted and smooth-varying Moho suggest that the mechanically strong mantle lithosphere and the crust respond differently to collision, with the upper crust currently undergoing pervasive strain over the entire plateau.

Introduction

How the lithosphere, comprises the whole crust and the uppermost part of the mantle, deforms over its entire thickness during continental collision is a first order question in geodynamics, as continental collision is a primary process responsible for assembling supercontinents and continental growth (Windley, 1995).

With an aperture of over 500 km, a dense station spacing of 5–10 km, and high signal-to-noise ratios (S/Ns), voluminous seismic data collected along the linear array of project Hi-CLIMB (Himalayan–Tibetan Continental Lithosphere during Mountain Building) (Nabelek *et al.*, 2005) offer an excellent opportunity to address continental deformation on a lithospheric scale across the most prominent zone of active continental collision—the Himalayan–Tibetan orogen. The aperture of the linear component of the array is sufficiently large to encompass both the Indus–Yarlung (IYS) and the Bangong–Nujiang (BNS) sutures in Tibet. The IYS is the surface join left by the latest episode of ongoing collision, which began in the Eocene, between the northern Indian shield and

the Lhasa terrane of southern Tibet, while the BNS marks a previous collision in the Jurassic–Cretaceous between the Lhasa terrane and the Qiangtang terrane in central Tibet (Yin and Harrison, 2000).

In the continental lithosphere, the most prominent, and thus potentially the most detectable feature is the Mohorovičić discontinuity (Moho), or the boundary between the Earth’s crust and the mantle where compositional change often causes a large contrast in seismic impedance. Using the Moho as a structural marker, previous studies reported features ranging from numerous, abrupt steps (up to 20 km in vertical offsets) in the Moho over a large region in southern Tibet (Hirn *et al.*, 1984), to an ill-defined interface with complex structures, to a gradual transition from the crust to the uppermost mantle (Owens and Zandt, 1997; Kind *et al.*, 2002; Hetényi *et al.*, 2007).

In this study, we match the dataset from the Hi-CLIMB array with seismic imaging of transmitted seismic-wave fields using Gaussian-beam (GB) migration to show that characteristics of the Moho are highly variable beneath the thickened crust of Tibet. While a sharp Moho, fluctuating little in depth and varying smoothly over hundreds of

*Now at Department of Geosciences, National Taiwan University, Taipei, Taiwan.

kilometers laterally, indicates stable blocks of mantle lithosphere beneath both the Lhasa and Qiangtang terranes, there is also a wide, intervening disrupted zone of the crust and Moho of about the same scale, suggesting pervasive deformation of the lithospheric mantle and the crust.

Teleseismic Phases Used for Imaging

At teleseismic distances, body waves generated by earthquakes reach a seismic station steeply from below and are approximately plane waves. Such an incident P wave will scatter into both P and S waves (with in-plane polarization, the SV phase) by strong impedance contrasts beneath a station, such as the Moho. The nomenclature of such scattered waves appears in most introductory texts of seismology (e.g., Stein and Wysession, 2003; fig. 6.3-7). For example, the P_s phase refers to a simple P to SV conversion, and the $PpPms$ phase is a P wave reflected under the Earth's surface and then converted to an SV wave from the topside of a buried scatterer. An incident SV wave also scatters into both P and SV waves beneath a seismic array.

Because of the thick crust in Tibet, multiple-scattered P waves within the crust (e.g., $PsPmp$) occur very late in the coda-wave train, and their amplitudes are typically weak. Consequently we focused our study based on the direct conversion of the P to S waves (the P_s phase). We tested using multiple reverberations in the data for imaging, but the results were less fruitful. However, along with the P_s phase, we also used a phase from S -wave scattering, $SsPmp$, to constrain the model for background seismic-wave speeds in the lithosphere used for imaging (Appendix B).

To form radial receiver functions, we use the vertical component of seismograms for a station–source pair as a reference to deconvolve the radial component in the frequency domain. This procedure effectively removes most of undesired effects from the source side, including history of earthquake rupture, plus scattering near the source and along the path of propagation, so that the forward scattered SV waves from the receiver side are emphasized. Moreover, the deconvolution normalizes the source time function, paving the way for further enhancement of the signal, such as stacking of data from several earthquakes at a given station.

Imaging of Teleseismic P -Wave Data Using Gaussian-Beam Migration

Seismic migration is a procedure that maps features observed on seismic profiles into appropriate subsurface locations of scatterers. A true scatterer must lie where the source-wave field, propagating from the source of illumination to the scatterers, and the observed wave field, backpropagated from the receivers to the scatterers, coincide (Claerbout, 1985). Under the Born approximation, this imaging condition is equivalent to applying the adjoint of linearized scattering operator to the scattered wave field (Tarantola, 2005).

We have chosen the GB approach to calculate the wave fields (Nowack *et al.*, 2006, 2007; Appendix A) for the migration and imaging of teleseismic P – S conversions, and this choice distinguishes our method from alternatives such as those of Bostock and Rondenay (1999) and Bostock *et al.* (2001), whose algorithms are based on geometric rays. A key advantage of the GB approach is its ability to handle triplicate (caustic) arrivals in the wave field without any special treatment. Such situations can arise not only in complex geologic settings but also in layered materials where strong seismic discontinuities, such as the Moho, are present. It turns out that complex structures that involve juxtaposition of materials with large impedance contrasts are apparent over considerable distances beneath the Hi-CLIMB linear array in Tibet, making GB migration an excellent technique of choice. In Appendix A, we demonstrate the success of this technique from a test designed specifically for this study. Furthermore, for seismic reflections in a highly complex setting, GB migration has been extensively validated by studies in geophysical exploration for some time (Hill, 1990, 2001).

The practice of migrating seismograms observed at each single location without considering neighboring observations (the common piercing-point [CPP] method) has been widely used (e.g., Schulte-Pelkum, 2005). In the CPP approach, the medium to be imaged is divided into a collection of cells. For each earthquake–station pair, segments of seismogram containing P -wave coda are assigned to cells where wave conversions are calculated to take place. Results for each cell are summed up for many earthquake–station pairs to form an image. This approach assumes one-dimensional (1D) structures for all calculations to construct two-dimensional (2D) images and then typically applies some arbitrary scheme to smooth the resulting product by averaging values from neighboring cells (bin averaging). In contrast to recent developments in imaging techniques (Bostock *et al.*, 2001; Nowack *et al.*, 2006, 2007), the CPP approach utilizes only a fraction of the information in the scattered wave field. The difference in methodology distinguishes the current study from other recent work (Hetényi *et al.*, 2007).

Application of Gaussian-Beam Migration to Hi-CLIMB Data in Tibet

In this study, the seismic sources are carefully selected to retain data with the best S/Ns and adequate azimuthal coverage, resulting in three groups of earthquakes. Each group covers a different quadrant of back azimuths and a restricted range in epicentral distances with respect to the Hi-CLIMB array (Fig. 1a). The southeastern group comprises 12 events, while the northeastern and the northwestern groups consist of 5 and 4 events, respectively (seismicity is too low in the southwestern quadrant to generate any suitable data). For each of the 75 stations, receiver functions from all events within a group are stacked to further enhance the S/R. In all, about 4275 seismograms are selected for analysis in the final dataset.

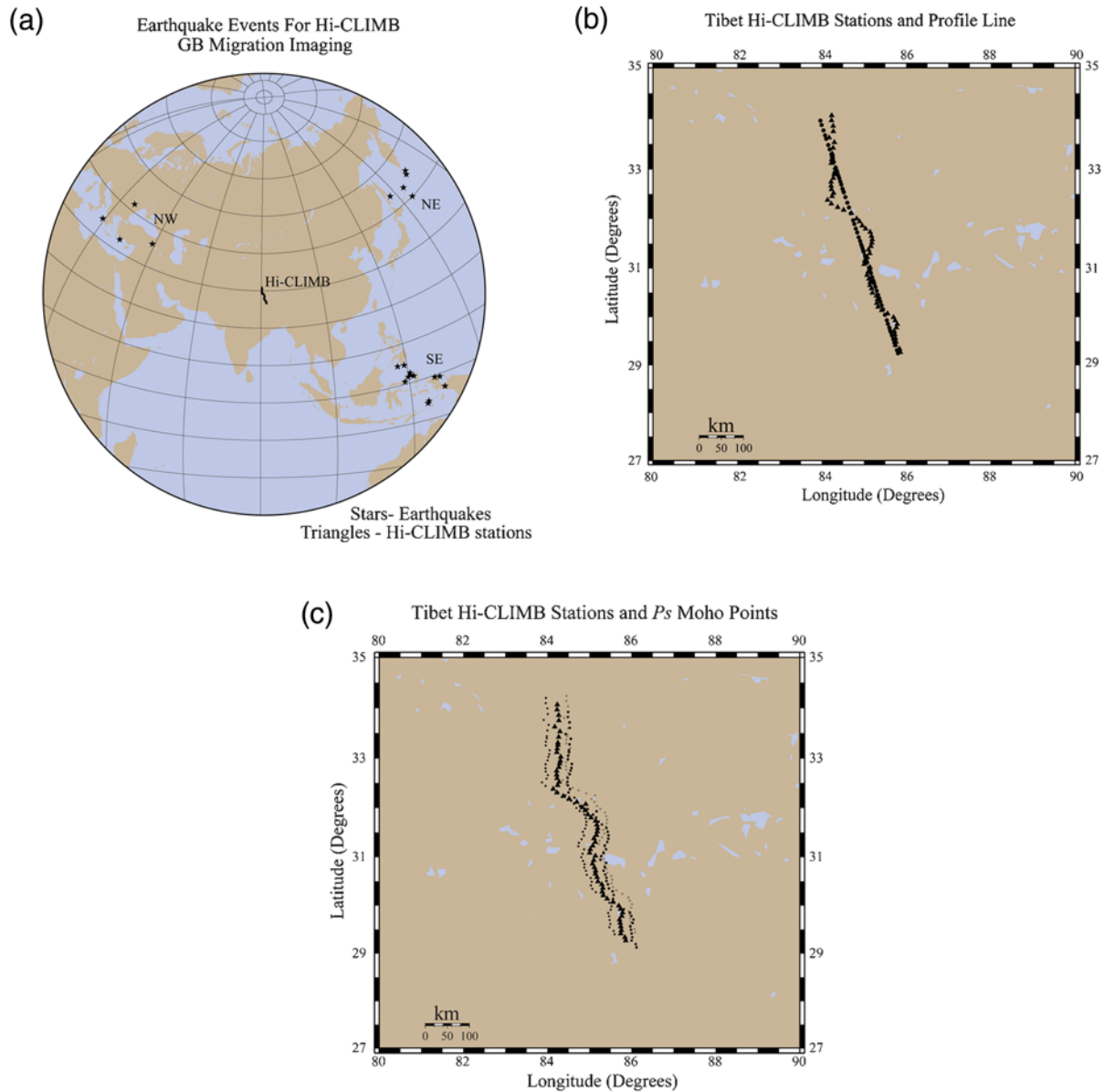


Figure 1. (a) A map showing epicenters of earthquake sources used for GB migration. The sources are carefully selected to retain data with the best S/Ns and to provide adequate coverage in back azimuths with respect to the Hi-CLIMB array. (b) A map showing locations of the Hi-CLIMB stations in central and southern Tibet (solid triangles), and their projected positions along a linear profile (solid circles). (c) A map showing locations of the Hi-CLIMB stations (solid triangles) and predicted locations of conversion points for the P_s phase assuming a constant Moho depths of 70 km (diamonds for the source group to the NW, crosses for the group to the NE, and circles for the group to the SE).

Next, a great circle is determined by a least-squares fitting of the locations of the stations, which are then projected onto the great circle to form a linear seismic profile (Fig. 1b). Finally we apply GB migration along this profile, adapting the GB method to accommodate irregular spacing among the stations along the line. Because of the irregular spacing of the data, the local slant stacking of the data as part of the GB migration is performed in the spatial domain, which avoids performing more elaborate trace interpolations. However, the resulting beam centers are regularly spaced along the profile (see Appendix A for further discussions on methodology). For the migration, the horizontal axis (x) is

set in kilometers along the profile (Fig. 1b) starting from the first station, H1000, at a projected position of 29.246° N and 85.804° E.

Given the fact that the array is approximately linear (Fig. 1), the GB algorithm we developed is 2D in nature, appropriate for a linear seismic profile. Our methodology does allow for the incident wave field to come from directions oblique to the profile. To help visualize the volume of lithosphere sampled along our profile, Figure 1c shows approximate locations of P_s conversion, assuming a constant Moho depth of 70 km, from all three azimuthal groups of earthquake sources. The conversion points form a swath

of about 25 km in width on each side of the array, outlining the limit of lateral coverage of the data. When images from all sources of illumination are stacked, average subsurface properties of any potential small scale, lateral variations within this swath are imaged onto the profile (see further discussions on Fresnel zones in the following section).

Gaussian-Beam Images from Individual Azimuths

In this section, we present the individual GB migration images using stacked seismic data from each of the three azimuths, southeast (SE), northeast (NE), and northwest (NW) of the array. Gaussian filters are chosen to minimize side lobes from filtering when receiver functions are formed, and the results are shown for three different Gaussian widths of $G_w = 0.90$ (low frequency), 1.25 (mid frequency), and 2.3 (high frequency), which correspond to reference frequencies of 0.24, 0.33, and 0.61 Hz where the Gaussian amplitude decreases to 0.5. Comparisons among these images illustrate the multiscale nature of scattering beneath the array.

Imaging algorithms require a background velocity model in order to determine the locations of the scatterers. For the Hi-CLIMB data, we use a 2D or laterally varying background model as described in Appendix B. We also tested laterally homogeneous models, and it turns out that the results of migration are not sensitive to specific details of the background velocity model. As noted before, we allow for the incident wave to propagate through the 2D model at the appropriate incident angle and azimuth for each event group. In doing so, data from different stations along the profile are aligned by the timing of the first P arrivals, and the timing of the incident wave field is correspondingly shifted.

Figure 2 shows the GB migration results based on stacked receiver functions from the 12 events located to the SE of the array (Fig. 1a). In all images, reflectivity of scatterers is normalized to a range between -1 and $+1$, with positive and negative values shown in blue and red colors, respectively. For reference, the locations of the IYS and BNS on the surface are also shown. The images cover the entire Lhasa terrane between the IYS and the BNS and the southern and central Qiantang terrane to about 200 km north of the BNS.

Between distances of 0 and 250 km, the low and mid frequency images at G_w of 0.9 and 1.25 (Fig. 2) show a coherent Moho scatterer at around 72 km in depth, with a short segment of disruption between distances of 120 and 150 km. Farther northward, the Moho is severely disrupted between distances from 250 to 350 km with enhanced lower crustal scattering. From 350 to 450 km reflectivity of the Moho is weak but then strengthens again between distances from 450 to 550 km at a somewhat shallower depth (by about 10 km). As expected, more complicated Moho structures appear in higher frequency images. At distances less than 250 km, a deeper scattering feature can be seen between 100 and 140 km in depth. Another deeper scattering structure can also be seen north of 300 km in distance and from 90 to 140 km in

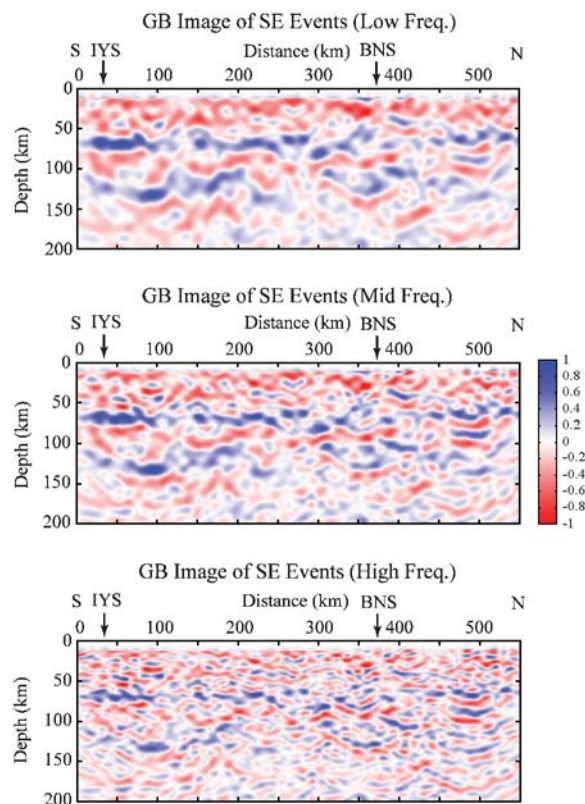


Figure 2. GB migration images formed by stacked receiver functions from 12 events to the SE of the Hi-CLIMB array shown in Figure 1a. The migration results are shown for three different Gaussian low-pass filters with Gaussian widths of $G_w = 0.90$ (low frequency), 1.25 (mid frequency), and 2.3 (high frequency). These values correspond to frequencies of 0.24, 0.33, and 0.61 Hz, where the amplitude of each filter drops by a factor of 2 of its peak value at 0 Hz.

depth, possibly dipping to the north. But these deeper scattering features could be false images related to multiples.

Figure 3 shows GB migration images for the NE stacked events at three different frequency bands. Similar to results from the SE, the Moho reflectivity is strong in the southern portion of the profile, appearing at a depth of about 72 km. The Moho becomes complicated between distances 225 and 300 km, and from 300 to 425 km reflectivity of the Moho is very subdued. The Moho scattering then strengthens north of about 450 km in distance and is about 10 km shallower in depth than that under the southern end of the profile. In contrast to the SE migration results, any structure deeper than the Moho, between depths of 100 and 150 km, is inconspicuous.

Finally, results from the NW events are shown in Figure 4. Note that both the quantity and quality of data in this azimuth are not as favorable as those of the other two groups. In Figure 4, Moho scattering is again strong in the southern portion of the profile, with some disruptions near the distance of 125 km but persists up to around 200 km, where it weakens. In contrast to the other two profiles, the Moho scattering is stronger between distances of 225 and up to the BNS but with some complicated midcrustal scattering.

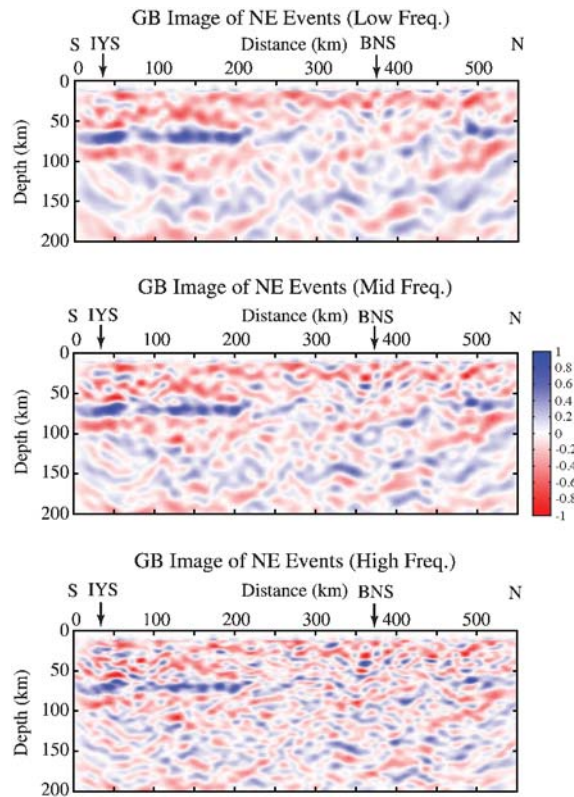


Figure 3. GB migration images formed by stacked receiver functions from five events to the NE of the Hi-CLIMB array shown in Figure 1a. The layout is the same as that in Figure 2.

Reflectivity of the Moho weakens between distances of 370 and 420 km and then strengthens again farther northward at a shallower depth. There appears to be some scattering below the Moho between depths of 100 and 180 km, but these features seem unstable, with considerable variations among different frequency bands.

Stacked Gaussian-Beam Images and Geologic Interpretations

Because successive collisions that built the Tibetan plateau are a result of northward convergence of fragments of the Gondwanaland toward stable Siberia (e.g., [Tapponnier et al., 2001](#)), the dominant trend of variation in geologic structures is north–south. Nevertheless, lateral variations, albeit at a smaller scale, are abundant (e.g., [Yin and Harrison, 2000](#)). Meanwhile, the geometry of the array is approximately 2D, so each group of events images somewhat different regions at depth, up to 25 km away from the projected position of the profile—a direct result of different incidence angles (mainly in azimuth) of the incoming P waves from below (Fig. 1c). For the range of dominant frequencies used here, the radii of the Fresnel zone at a depth of 70 km are about 14–23 km. These values are comparable to the half-width of the swath of conversion points straddling the array (Fig. 1c), calling for geological interpretations to rely upon stacked images from all three azimuthal groups of sources.

(Nonetheless, notice that horizontal resolution along the profile is high, on the order of 8 km or less as illustrated by tests with synthetic seismograms, Appendix A, Fig. A2).

Furthermore, because a seismic deployment at the scale of Hi-CLIMB is by necessity a temporary endeavor, this constraint limits the azimuthal coverage of data due to the intrinsic geometry and nonstationary nature of the Earth’s seismicity. As such, instead of appealing to exotic explanations that cannot be verified by existing data, we attribute any apparent azimuthal variations in our results to slight deviations from a purely 2D geometry of geologic structures within the swath of conversion points around the array. As such, we perform final interpretations based on linear stacking of images from the three available azimuths (Fig. 5), bearing in mind the fact that the overall data quality and quantity are best for the events from the SE and NE of the array.

Before proceeding with the final interpretation, it is heuristic to recall that in addition to the great depth of penetration from wave fields generated by large earthquakes, the broadband nature of signals from earthquakes is important. First, gradual changes in impedance are not particularly sensitive to high-frequency waves, a common issue for earlier studies in southern Tibet that rely on man-made sources of illumination ([Hauck et al., 1998](#)). Second, as spatial resolution increases with increasing frequency, so does the complexity of the resulting image. Comparison among the images from

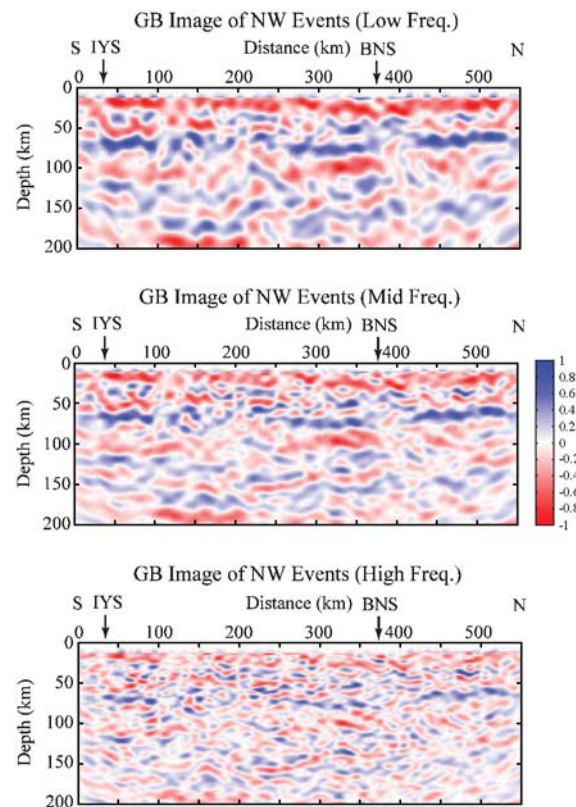


Figure 4. GB migration images formed by stacked receiver functions from four events to the NW of the Hi-CLIMB array shown in Figure 1a. The layout is the same as that in Figure 2.

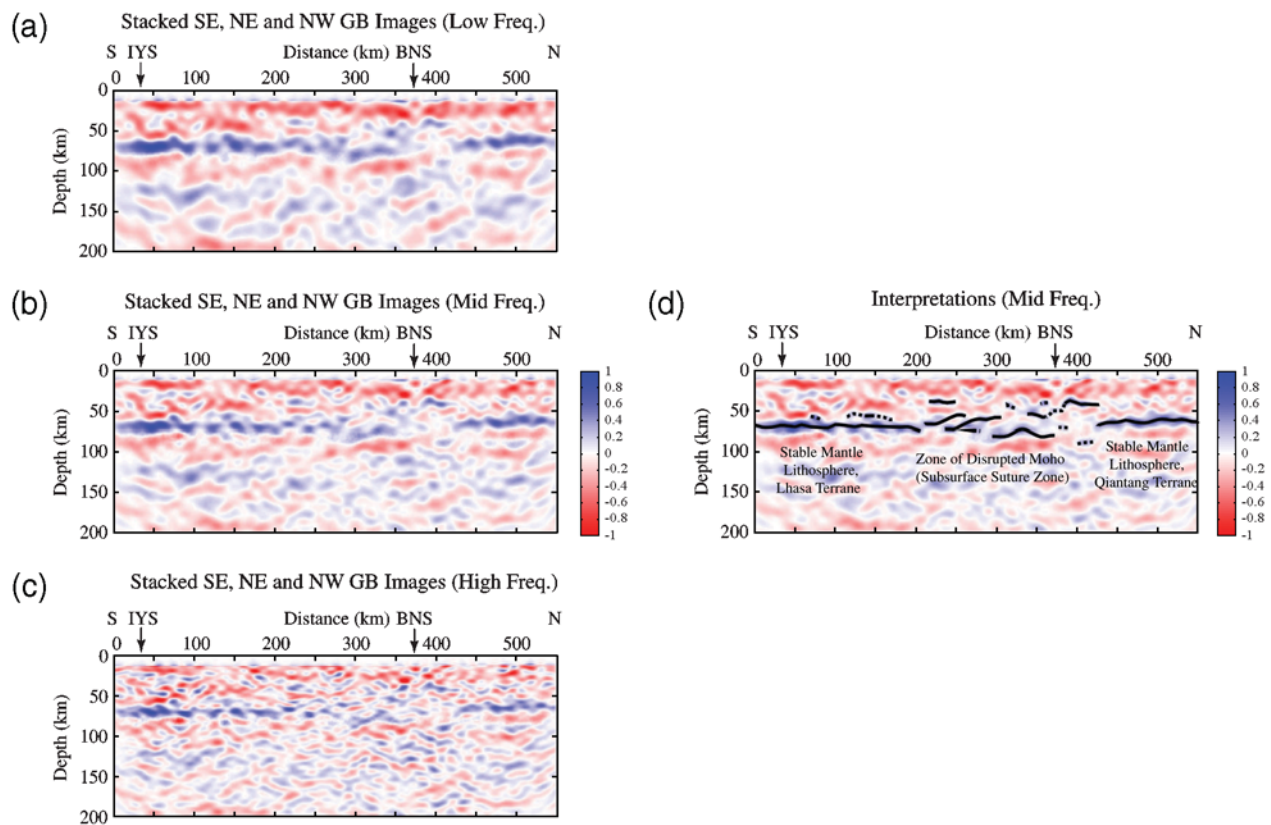


Figure 5. Cross sections of the Tibetan lithosphere as imaged by GB migration of direct P -to- S wave conversions. The images are stacked from three basic images corresponding to sources from the SE, the NE, and the NW of the array (Figs. 2–4). The convention is that a scatterer representing an increase in impedance with depth results in a blue pixel centered on the position of the scatterer. (a)–(c) Facilitated by the broadband nature of earthquake data, these images are formed at three different frequency bands. Prior to migration, signals are filtered with low-pass Gaussian filters characterized by Gaussian widths of 0.90 (low frequency), 1.25 (mid frequency), and 2.30 (high frequency). The layout is the same as that in Figure 2. (d) Same image as in (b), with our interpretations of the Moho transition zone highlighted by black curves (dashed when uncertain).

different frequencies allows geologic interpretations that achieve a balance between high resolution and lateral continuity of feature. To this end, the image from the midfrequency band works well. Note that we applied no smoothing to either the pre- or postmigrated images.

As expected, the strongest signal comes from the Moho in the stacked images—a feature that is well imaged in all frequency bands (Fig. 5a–c). More important, characteristics of the Moho vary considerably over the profile. Near both ends of the profile, the Moho is a sharp, continuous interface, with a noticeable difference of about 10 km in crustal thickness. The difference in crustal thickness is important for understanding how uniform, high elevation of central and Northern Tibet is being supported (see Tseng *et al.*, 2009, for further discussions). Near a distance (x) of about 100 km (Fig. 5), there appears to be a slight break in its continuity but otherwise the Moho interface remains a well-defined, laterally continuous feature that shows only minor fluctuations for another 100 km. However, between $x = 200$ and 430 km, a wide zone of disrupted Moho stands out. Even at low frequencies (Fig. 5a), it is apparent that the Moho is disrupted; instead the crust–mantle transition spans a large range of depths from about 80 to 40 km. Figure 5d shows our interpretation

of the current configuration of the Moho for the entire profile by highlighting scatterers with particularly strong impedance contrast. Some of the details at depth are resolvable only at high frequencies. For instance, apparent imbrications of the Moho near a distance of 250 km are best seen in Figure 5b,c.

As a first approximation, we assume that the properties of the uppermost mantle are homogeneous and isotropic. Possible deviations from this approximation, such as fluctuations in the speed of mantle P waves, will affect the precise interpretation of the impedance contrast across the Moho, but positions of the prominent scatterers are not sensitive to the details of the background seismic-wave speeds (see Appendix B for further discussion).

Traditionally, identification of a suture between two colliding terranes is based on observations near the surface, characterized by a broad zone of allochthonous terranes, including fragments of exotic terranes, oceanic rocks, and accretionary prisms from both sides of the main intervening ocean. Consequently, the precise location of a complex suture zone is often nonunique, because the answer depends on whether structural features (including ophiolites), patterns of isotopic ratios, or paleontological criteria are used

(Windley, 1995). On a lithospheric scale, the subsurface or geophysical suture is the subsurface join between opposing, stable terranes (Marillier, 1989). In our case, it is straightforward to identify sharp, flat-lying portions of the Moho toward the southern and northern ends of the cross section as stable mantle lithosphere of Lhasa and Qiangtang terranes, respectively (Fig. 5d).

The fact that disrupted (therefore deformed) Moho is limited to the central portion of the profile points to considerable strength of the mantle lithosphere. If the mechanical strength of the entire lithosphere mainly resides in the crust (“crème brûlée”) (e.g., Jackson, 2002), deformation of the Moho should be as pervasive and widespread as the crust whose top surface is undergoing significant pure shear throughout the entire plateau (Meade, 2007; Thatcher, 2007). A strong lithospheric mantle is consistent with independent evidence from the occurrence of mantle earthquakes in southern Tibet (Chen and Molnar, 1983; Chen and Yang, 2004; de la Torre, 2007), favoring a bimodal distribution of lithospheric strength with maxima in the midcrust and near the Moho (“jelly sandwich”).

Interestingly, the zone of disturbed Moho straddles the BNS, but there is no corresponding feature under the IYS. Such a difference suggests that the zone of disturbance near the BNS has been reworked during the most recent episode of collision and/or different processes that occurred during the two successive episodes of collision. An obvious piece of supporting evidence for the latter is the differences in the distribution of rocks and geologic structures near the surface. While the Lhasa terrane is largely covered by both eruptive volcanism and large granitic plutons that mark the active continental margin prior to collision along the IYS (Yin and Harrison, 2000), the Qiangtang terrane is an anticlinorium with Mesozoic blueschist-bearing mélangé and upper Paleozoic strata in the core (Kapp *et al.*, 2005). Tapponnier *et al.* (2001) proposed that the BNS is associated with southward underthrust of the Qiangtang terrane (intracontinental subduction), while Kapp *et al.* (2005) emphasized contraction, with north-dipping imbricate thrust sheets near the surface and uniform crustal thickening at depth. Apparent imbrications of the Moho suggest that south-dipping thrust faulting of the uppermost mantle could be involved (Fig. 5), a process currently active beneath the Himalayan deformation front except that there the dip direction of the entire system is toward the north (Chen and Kao, 1996).

The occurrence of more than one large impedance contrast in the zone of disrupted Moho could suggest that mafic, or even ultramafic, mantle materials have been incorporated into the thickened crust and some mantle materials now reside in the mid- to lower crust (Fig. 5). This interpretation is supported by field evidence from mature collision zones where erosion has exposed the deep anatomy of thickened crust. For instance, in the Norwegian Caledonide, a product of early Paleozoic collision between Baltica and Laurentia, van Roermund *et al.* (1998) and Scambelluri *et al.* (2008) reported detailed studies of the Ugelvik–Raudhaugene–

Midsundvattnet peridotite bodies in the Western Gneiss region of Norway. This ultramafic body, originally emplaced at the mid- to lower crustal level, is now exposed at the surface within a highly metamorphosed continental crust where the Moho is currently at a depth of about 35 km (Artemieva and Thybo, 2008). In Norway alone, there are numerous other examples of known ultramafic bodies in deformed continental crust (Brueckner and van Roermund, 2004).

There has been a long-standing debate as to whether diffuse deformation, a characteristic of continental lithosphere, is best explained as interaction among discrete blocks (Tapponnier *et al.*, 2001; Calais, *et al.*, 2006) or deformation of a continuous medium (Houseman and England, 1993; Holt *et al.*, 2000). Space-based geodetic measurements indicate that on a scale of ~100 km or more, the surface of Tibet is currently under uniform strain (Meade, 2007; Thatcher, 2007), with subsidiary contribution from motion across discrete faults. At depths of about 70 km beneath the thickened crust, our results show that there are stable blocks in the mantle portions of the lithosphere beneath both the Qiangtang and Lhasa terranes where the Moho is a laterally continuous, smooth-varying feature, visible via both high- and low-frequency seismic waves (Fig. 5c). Between the two stable blocks is a wide zone of highly disrupted Moho, of comparable scale to that of the stable blocks (~200 km). This observation suggests that for the mantle lithosphere, the motion of discrete blocks and pervasive deformation over wide intervening zones are of about equal importance.

Conclusions

We applied GB migration of teleseismic *P* waves to image the lithosphere in Tibet using data from the linear array of the Hi-CLIMB experiment. We selected three-component *P*-wave data from three groups of earthquakes, each within a restricted range of azimuth and distance, to form stacks of radial receiver functions that we then used to image the lithosphere by GB migration. The broad bandwidth of the data facilitates imaging at different frequency bands for each azimuth, constraining multiscale scattering properties of the lithosphere. For each frequency band, images from each group of illumination are then stacked to form a final GB image for geologic interpretations.

Overall, heterogeneities beneath a wide zone of about 250 km in length near the BNS in the heartland of Tibet are more pronounced than those under apparently stable terranes farther to the south or the north. Specifically, *P*-to-*S* conversions across the Moho are generally strong and continuous under much of the southern Lhasa terrane, corresponding to a well-defined Moho. A disrupted zone of the Moho and strong crustal scattering appear in the vicinity of the BNS. The disrupted zone marks the subsurface join of stable portions of mantle lithosphere of considerable mechanical strength under southern and central Tibet. At the northern end of profile in the Qiangtang terrane, the Moho shoals in depth and there is also an increase in Moho reflectivity.

Similar length scales of about 200 km between regions with disrupted and smooth-varying Moho suggest that the strong mantle lithosphere and the crust respond differently to collision, with the upper crust currently undergoing pervasive strain over the entire plateau.

Data and Resources

Seismic data used in this study were collected as part of the Hi-CLIMB Project using a variety of instruments, including many from the Incorporated Research Institutions in Seismology–Program for the Array Seismic Studies of the Continental Lithosphere (IRIS–PASSCAL) Center. The project was organized and coordinated jointly by the University of Illinois (principal investigator, Wang-Ping Chen) and the Oregon State University (principal investigator, John Nabelek). Seismic data can be obtained directly from the IRIS Data Management Center at www.iris.edu.

References

- Artemieva, I. M., and H. Thybo (2008). Deep Norden: Highlights of the lithospheric structure of northern Europe, Iceland, and Greenland, *Episodes* **31**, 98–106.
- Bleistein, N. (2009). Mathematics of modeling, migration and inversion with Gaussian beams, Lecture Notes, www.cwp.mines.edu/~norm/ (last accessed September 2009).
- Bostock, M. G., and S. Rondenay (1999). Migration of scattered teleseismic body waves, *Geophys. J. Int.* **137**, 732–746.
- Bostock, M. G., S. Rondenay, and J. Shragge (2001). Multiparameter two-dimensional inversion of scattered teleseismic body waves 1. Theory for oblique incidence, *J. Geophys. Res.* **106**, 30,771–30,782.
- Brueckner, H. K., and H. L. M. van Roermund (2004). Dunk tectonics: A multiple subduction/duction model for the evolution of the Scandinavian Caledonides, *Tectonics* **23**, doi [10.1029/2003TC001502](https://doi.org/10.1029/2003TC001502).
- Calais, E., L. Dong, M. Wang, Z. Shen, and M. Vergnolle (2006). Continental deformation in Asia from a combined GPS solution, *Geophys. Res. Lett.* **33**, doi [10.1029/2006GL028433](https://doi.org/10.1029/2006GL028433).
- Cerveny, V., M. M. Popov, and I. Psencik (1982). Computation of wavefields in inhomogeneous media—Gaussian beam approach, *Geophys. J. R. Astr. Soc.* **70**, 109–128.
- Chen, W.-P., and H. Kao (1996). Seismotectonics of Asia: Some recent progress, in *The Tectonic Evolution of Asia*, A. Yin and M. Harrison (Editors), Cambridge U Press, New York, 37–62.
- Chen, W.-P., and P. Molnar (1983). Focal depths of intraplate and intraplate earthquakes and their implications for the thermal and mechanical properties of the lithosphere, *J. Geophys. Res.* **88**, 4183–4214.
- Chen, W.-P., and Z. H. Yang (2004). Earthquakes beneath the Himalayas and Tibet: Evidence for strong lithospheric mantle, *Science* **304**, 1949–1952.
- Claerbout, J. F. (1985). *Imaging the Earth's Interior*, Blackwell, Oxford.
- de la Torre, T. L., G. Monsalve, A. F. Sheehan, S. Sapkota, and F. Wu (2007). Earthquake processes of the Himalayan collision zone in eastern Nepal and the southern Tibetan Plateau, *Geophys. J. Int.* **171**, 718–738.
- Hauck, M. L., K. D. Nelson, L. D. Brown, W. Zhao, and A. R. Ross (1998). Crustal structure of the Himalayan orogen at similar to 90 degrees east longitude from Project INDEPTH deep reflection profiles, *Tectonics* **17**, 481–500.
- Hetényi, G., R. Cattin, F. Brunet, L. Bollinger, J. Vergne, J. Nabelek, and M. Diament (2007). Density distribution of the India plate beneath the Tibetan plateau: Geophysical and petrological constraints on the kinetics of lower-crustal eclogitization, *Earth Planet. Sci. Lett.* **264**, 226–244.
- Hill, N. R. (1990). Gaussian beam migration, *Geophysics* **55**, 1416–1428.
- Hill, N. R. (2001). Prestack Gaussian beam depth migration, *Geophysics* **66**, 1240–1250.
- Hirn, A., A. Necessian, M. Sapin, G. Jobert, Z. X. Xu, E. Y. Gao, D. Y. Lu, and J. W. Teng (1984). Lhasa block and bordering structures—A continuation of a 500-km Moho traverse through Tibet, *Nature* **307**, 25–27.
- Holt, W. E., N. Chamotrooke, X. Le Pichon, A. J. Haines, B. Shen-Tu, and J. Ren (2000). Velocity field in Asia inferred from Quaternary fault slip rates and global positioning system observations, *J. Geophys. Res.* **105**, 19,185–19,209.
- Houseman, G., and P. England (1993). Crustal thickening versus lateral expulsion in the Indian–Asian continental collision, *J. Geophys. Res.* **98**, 12,233–12,249.
- Jackson, J. (2002). Strength of the continental lithosphere: Time to abandon the jelly sandwich?, *GSA Today* **12**, 4–10.
- Kapp, P., A. Yin, T. M. Harrison, and L. Ding (2005). Cretaceous–Tertiary shortening, basin development and volcanism in central Tibet, *Geol. Soc. Am. Bull.* **117**, 865–878.
- Kind, R., X. Yuan, J. Saul, D. Nelson, S. V. Sobolev, J. Mechie, W. Zhao, G. Kosarev, J. Ni, U. Achauer, and M. Jiang (2002). Seismic images of crust and upper mantle beneath Tibet: Evidence for Eurasia plate subduction, *Science* **298**, 1219–1221.
- Marillier, F., C. E. Keen, G. S. Stockmal, G. Quinlan, H. Williams, S. P. Colmansadd, and S. J. O'Brien (1989). Crustal structure and surface zonation of the Canadian Appalachians—Implications of deep seismic-reflection data, *Can. J. Earth Sci.* **26**, 305–321.
- Meade, B. J. (2007). Present-day kinematics at the India–Asia collision zone, *Geology* **35**, 81–84.
- Mejia, J. A. (2001). Lithospheric structure beneath the Tibetan plateau using simultaneous inversion of surface wave dispersion and receiver functions, *Ph.D. Thesis*, Saint Louis University.
- Nabelek, J., W.-P. Chen, M. R. Pandey, J. Mei, J. Chen, B.-S. Huang, and The Project HiCLIMB Team (2005). A high-resolution seismic profile across the Himalayas and southern Tibet, *IRIS Annual Report*.
- Nowack, R. L. (2003). Calculation of synthetic seismograms with Gaussian beams, *Pure Appl. Geophys.* **160**, 487–507.
- Nowack, R. L., and K. Aki (1984). The two-dimensional Gaussian beam synthetic method: Testing and application, *J. Geophys. Res.* **89**, 7797–7819.
- Nowack, R. L., W. P. Chen, U. Kruse, and S. Dasgupta (2007). Imaging offsets in the Moho: Synthetic tests using Gaussian beams with teleseismic waves, *Pure Appl. Geophys.* **164**, 1921–1936.
- Nowack, R. L., S. Dasgupta, G. T. Schuster, and J. M. Sheng (2006). Correlation migration using Gaussian beams of scattered teleseismic body waves, *Bull. Seismol. Soc. Am.* **96**, 1–10.
- Owens, T. J., and G. Zandt (1997). Implications of crustal property variations for models of Tibetan Plateau evolution, *Nature* **387**, 37–43.
- Popov, M. M. (1982). A new method of computation of wave fields using Gaussian beams, *Wave Motion* **4**, 85–97.
- Popov, M. M. (2002). *Ray Theory and Gaussian Beam Method for Geophysicists*, Lecture Notes, University of Bahia, Salvador Brazil, 172 pp.
- Rapine, R., F. Tilmann, M. West, J. Ni, and A. Rodgers (2003). Crustal structure of northern and southern Tibet from surface wave dispersion analysis, *J. Geophys. Res.* **108**, no. B2, doi [10.1029/2001JB000445](https://doi.org/10.1029/2001JB000445).
- Scambelluri, M., T. Petke, and H. L. M. van Roermund (2008). Majoritic garnets monitor deep subduction fluid flow and mantle dynamics, *Geology* **36**, 59–62.
- Schulte-Pelkum, V., G. Monsalve, A. Sheehan, M. R. Pandey, S. Sapkota, R. Bilham, and F. Wu (2005). Imaging the Indian subcontinent beneath the Himalaya, *Nature* **435**, 1222–1225.
- Shapiro, N. M., M. H. Ritzwoller, P. Molnar, and V. Levin (2004). Thinning and flow of Tibetan crust constrained by seismic anisotropy, *Science* **305**, 233–236.
- Stein, S., and M. Wysession (2003). *An Introduction to Seismology, Earthquakes and Earth Structure*, Blackwell, Oxford.

- Tapponnier, P., Z. Q. Xu, F. Roger, B. Meyer, N. Arnaud, G. Wittlinger, and J. S. Yang (2001). Oblique stepwise rise and growth of the Tibet plateau, *Science* **294**, 1671–1677.
- Tarantola, A. (2005). *Inverse Problem Theory and Methods for Model Parameter Estimation*, SIAM, Philadelphia.
- Thatcher, W. (2007). Microplate model for the present-day deformation of Tibet, *J. Geophys. Res.* **112**, B01401, doi [10.1029/2005JB004244](https://doi.org/10.1029/2005JB004244).
- Tseng, T. L., W. P. Chen, and R. L. Nowack (2009). Northward thinning of Tibetan crust revealed by virtual seismic profiles, *Geophys. Res. Lett.* **36**, L24304, doi [10.1029/2009GL040457](https://doi.org/10.1029/2009GL040457).
- van Roermund, H. L. M., and M. R. Drury (1998). Ultra-high pressure ($P > 6$ GPa) garnet peridotites in western Norway: Exhumation of mantle rocks from > 185 km depth, *Terra Nova* **10**, 295–301.
- Windley, B. F. (1995). *Evolving Continents*, Wiley, New York.
- Yin, A., and T. M. Harrison (2000). Geologic evolution of the Himalayan–Tibetan orogen, *Annu. Rev. Earth Planet. Sci.* **28**, 211–280.
- Zhao, W., J. Mechie, L. D. Brown, J. Guo, S. Haines, T. Hearn, S. L. Klempner, Y. S. Ma, R. Meissner, K. D. Nelson, J. F. Ni, P. Pananont, R. Rapine, A. Ross, and J. Saul (2001). Crustal structure of central Tibet as derived from project INDEPTH wide-angle seismic data, *Geophys. J. Int.* **145**, 486–498.
- Zhu, L. (1998). Broadband waveform modeling and its application to the lithospheric structure of the Tibetan plateau, *Ph.D. Thesis*, California Institute of Technology.
- Zhu, L., and H. Kanamori (2000). Moho depth variation in southern California from teleseismic receiver functions, *J. Geophys. Res.* **105**, 2969–2980.

Appendix A

Gaussian-Beam Migration Using Teleseismic Body Waves

Here we give a brief overview of the imaging technique used in this study, GB migration (detailed discussions appear in [Nowack et al., 2006, 2007](#), and references therein). In a

heterogeneous elastic medium, the Green's function for a propagating wave can be expanded as a sum of Gaussian beams ([Cerveny et al., 1982](#); [Popov, 1982](#); [Nowack and Aki, 1984](#); [Popov, 2002](#); [Nowack, 2003](#); [Bleistein, 2009](#)). Each individual beam is expressed as a complex function of amplitude and phase, where the beam amplitude includes geometric spreading, reflection/transmission coefficients, ray-dependent radiation patterns of the source, and polarization vectors specified at positions along the beam's central ray. One important feature of the Gaussian beam is that although the term for geometric spreading is complex, it remains nonsingular along the entire beam even at caustics that would require complicated, special treatment in purely ray-based methods ([Bostock et al., 2001](#)).

To form a beam-based solution, the complex phase term is expanded to second order for locations surrounding the central ray of the beam. The curvature matrix, devised to describe the phase away from the central ray, is complex and positive definite; its real part represents the curvature of the wavefront, while the imaginary part tapers the amplitude away from the central ray to form a beam. At locations off the central ray, applying a paraxial or second-order approximation of the phase term eliminates the need for two-point ray tracing, resulting in a significant reduction of computations.

For the task at hand, the scattered SV-wave field data recorded at the surface are windowed with a set of overlapping Gaussian window functions at discrete positions in the distance. Figure [A1a](#) schematically displays a Gaussian window function that is applied to the data. The windowed data are then processed using local slant stacks to form a set of beam elements of the data as a function of beam center, X , and angle, θ . Paraxial Gaussian beams are used to backpropagate the

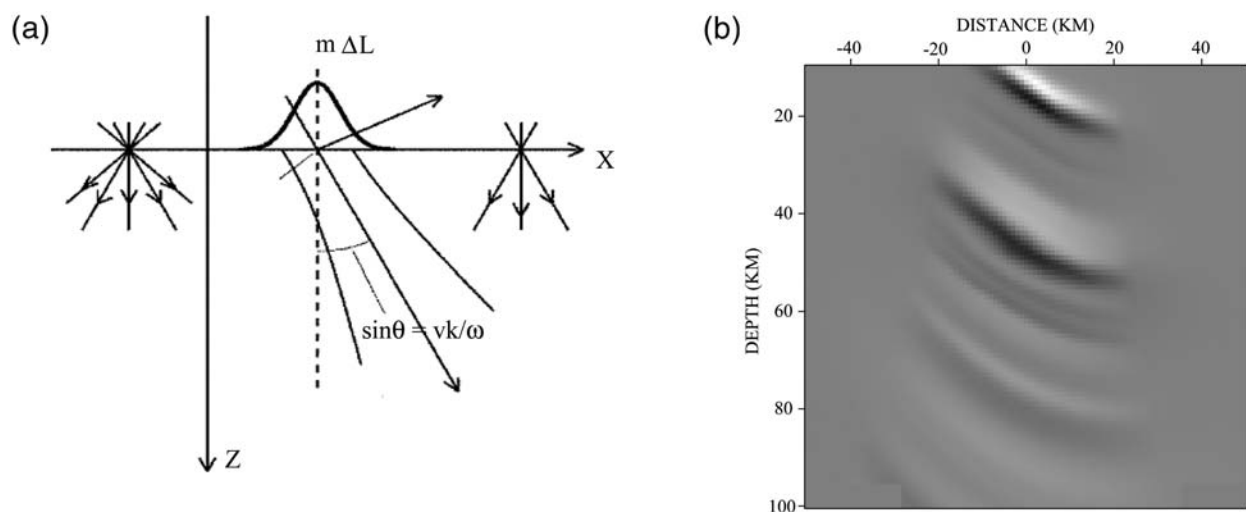


Figure A1 (a) A schematic diagram of a Gaussian window that is applied to the wave-field data recorded at the surface ([Nowack et al., 2007](#)). A local slant stack is applied to each window of the data to form a set of initial beam elements as a function of beam center, X , and angle, θ . Paraxial Gaussian beams are used to backpropagate the individual beam elements of the data into the subsurface. At each position in the subsurface, the backpropagated beam elements are cross correlated with the incident wave field, and then the results are integrated over frequency to form the final image. (b) An example of GB imaging using only a single beam element to represent a fraction of the scattered SV-wave field from a near-vertical, incident P wave. The target structure is an overhang in the Moho, already emerging from this incomplete image ([Nowack et al., 2007](#)).

individual beam elements of the data into the subsurface. At each position in the subsurface, the backpropagated beam elements are cross correlated with the incident wavefield, and then the results are integrated over frequency to form the final image.

This formulation is similar to that of Hill (2001) originally designed for prestack migration of seismic reflection data but is now extended to scattered *SV* waves associated with upgoing, incident *P* waves from distant earthquakes. To help visualize how GB migration works, Figure A1b shows an example using synthetic seismograms calculated for a model of thickened crust, with a sharp overhang in the Moho between depths of 40 and 55 km (Nowack *et al.*, 2007). The target is illuminated by a planar *P* wave whose initial angle of incidence is 15° counterclockwise from the vertical. Between depths of about 40 and 60 km, an incomplete image, mostly for the dipping portion of the Moho, already begins forming by using only the image formed by a single beam. When a full set of beams is applied, the resulting image faithfully

depicted the Moho, including the sharp overhang that separates two regions of different crustal thickness (40 km versus 55 km; Nowack *et al.*, 2007).

The GB imaging algorithm was further tested using synthetic receiver functions, generated for a linear array comprises 75 stations at a station spacing of 7.5 km—a configuration similar to the Hi-CLIMB array in Tibet. The input model of scatterers follows the interpreted positions of the Moho shown in Figure 5d, and the resulting synthetic receiver functions are shown Figure A2a, where the direct *P*-wave pulse has been muted out (which would otherwise appear at 0 sec on the plot).

The synthetic seismograms are calculated with a ray-theory based method under the Born approximation, using a Ricker wavelet as the incident *P* pulse whose initial angle of incidence at the surface is 24° clockwise from the vertical. Contrary to processing of the actual data, the source wavelet is prescribed so that the radial component of the synthetic seismograms are the desired radial receiver functions without

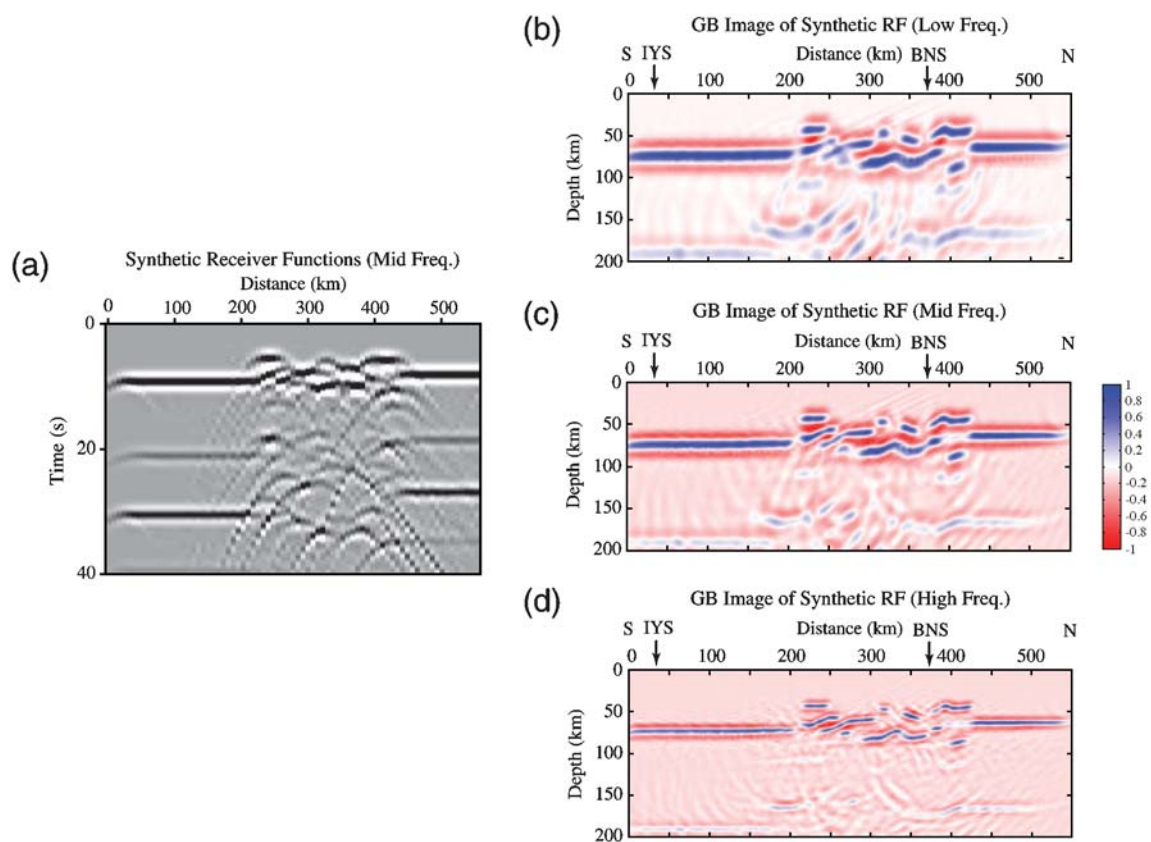


Figure A2. An example of GB imaging using synthetic seismograms. (a) Ray-theoretical synthetic receiver functions under the Born approximation. Scatterers representing the crust–mantle transition are placed in a configuration to simulate our interpretation of results shown in Figure 5d. For clarity, the direct *P* wavelet has been muted (which would otherwise arrive at 0 sec). The earliest arrivals shown are from the *P_s* phase, and later arrivals are multiples or reverberations in the crust. Notice pronounced hyperbolic patterns due to diffraction. The input pulse is a Ricker wavelet at three different bands with predominant frequencies of 0.24 Hz (low frequency), 0.33 Hz (mid frequency), and 0.61 Hz (high frequency); resulting images from GB migration of the *P_s* phase are shown in panels (b), (c), and (d), respectively. (b)–(d) Result of GB migration at three frequency bands. In all case, key features of the input model are faithfully imaged. Weak features that appear at depths greater than 70 km below the Moho are false images due to reverberations in the crust, arriving late in the synthetic seismograms, that do not meet imaging conditions designed only for the *P_s* phase.

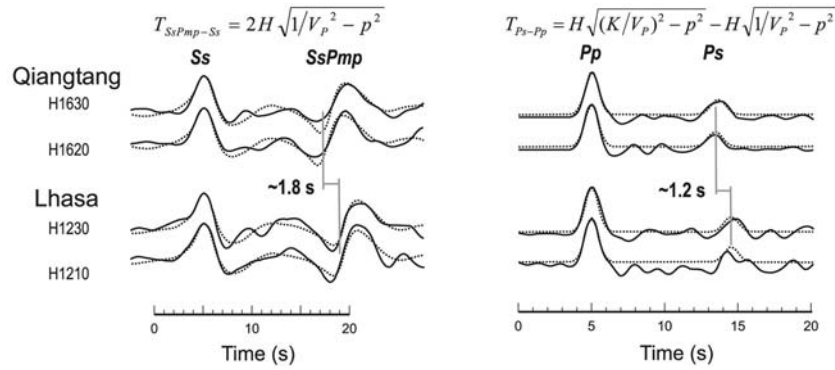


Figure B1. Comparison between observed (solid traces) and synthetic waveforms (dotted traces) for representative stations in central Lhasa and Qiangtang terranes, using preferred values of parameters indicated in Table B1. Both *S*-to-*P* wave conversions (left-hand panel, vertical component of ground velocity) and *P*-to-*S* wave conversions (right-hand panel, deconvolved radial component of seismograms) are simultaneously matched by the synthetic seismograms. Notice obvious differences in timing of converted phases for different terranes. The top row shows key equations (see text for definitions of symbols).

the need for any deconvolution. In Figure A2a, the earliest packet of arrivals corresponds to *Ps* phase from the Moho, and the later packets are multiple-scattered arrivals (reverberations) within the crust. Notice clear, hyperbolic patterns due to diffraction near edges of segmented Moho in the central portion of the plot.

The migrated images of the *Ps* phase are shown in Figure A2b–d for three different bands of frequencies. The dominant frequency at each band is approximately the same as the low-pass frequency of the corresponding bands used in Figure 5. While Ricker wavelets used in this synthetic example cause increased side lobes in the resulting images, salient features of the input model, including the complex zone of disrupted Moho, are successfully recovered by GB migration. (Faint features below the Moho, at depths greater than 70 km are ghosts from reverberations in the data not accounted for

by the imaging condition that is appropriate only for the *Ps* phase.) This test is particularly reassuring in that although according to strict, theoretical limits, the synthetic data are slightly aliased given the station spacing and frequency content being considered—characteristics similar to the observed data—key features of the Moho are still effectively reconstructed by GB migration.

Appendix B

Reference Crustal Models

The relationship for differential timing between phases *Ps* and *Pp* (T_{Ps-Pp}) and crustal thickness (H) is

$$T_{Ps-Pp} = H\sqrt{(K/V_p)^2 - p_\alpha^2} - H\sqrt{1/V_p^2 - p_\alpha^2}, \quad (\text{B1})$$

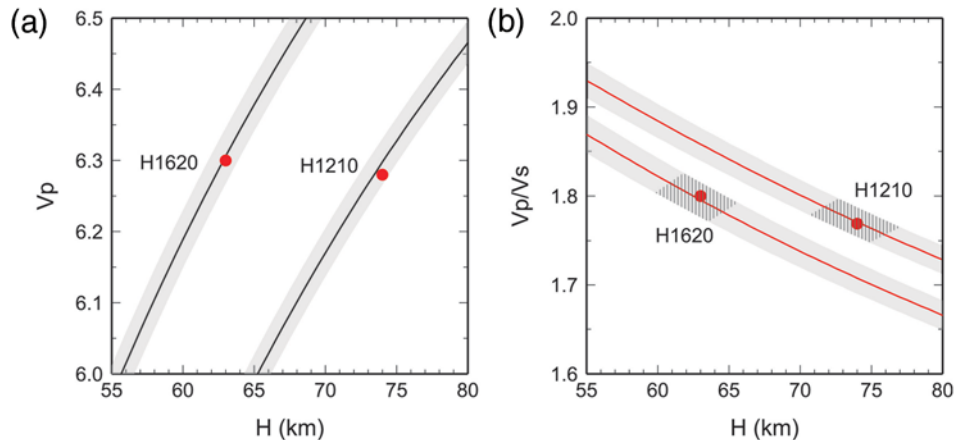


Figure B2. (a) Relationship between V_p and H based on differential timing of *SsPmp-Ss* (which is independent of V_s). Labels “H1210” and “H1620” mark possible solutions (solid curves) for stations representative of the Lhasa and Qiangtang terranes, respectively. Gray bands indicate the effect from errors of ± 0.2 sec in relative timing. Red dots represent preferred values used for waveform modeling shown in Figure B1. (b) Relationship between K and H by combining acceptable values of V_p and H in (a) and observed differential timing of *Ps-Pp*. The layout is the same as in (a), with hatched zones marking the effect from variations of ± 0.05 km/sec in V_s along the gray bands. This plot is not to be confused with similar-looking diagrams such as those in Zhu and Kanamori (2000) where the value of V_p is assumed to be known.

Table B1
Reference Model for Migration

Distance (km)	P-Wave Speed (V_P , in km/sec)	S-Wave Speed (V_S , in km/sec)	Average Thickness (H , in km)
Crust			
0–290 (Lhasa terrane)	6.28	3.55	74.0
290–393 (transition)		linear interpolations	
393–551 (Qiangtang terrane)	6.30	3.50	63.0
Mantle			
0–551	8.1	4.6	half-space

where p_α is the ray parameter of the incident P wave, and K is the ratio between average P - and S -wave speeds in the crust, or V_P/V_S (Zhu and Kanamori, 2000). In all, there are three unknowns: V_P , V_S , and H . To obtain the appropriate value of each parameter, first we add a constraint from differential timing $T_{SsPmp-Ss}$, taking advantage of the fact that the phase $SsPmp$ has very large amplitude (Fig. B1), often resulting in outstanding S/N s (Tseng *et al.*, 2009). Notice that $T_{SsPmp-Ss}$ is independent of V_S :

$$T_{SsPmp-Ss} = 2H\sqrt{1/V_P^2 - p_\beta^2}, \quad (\text{B2})$$

where p_β is the ray parameter of the incident S wave. Second we limit solutions for H to the range within which corresponding values of V_S satisfy constraints from surface-wave studies.

Figure B1 shows the result of waveform modeling for two sets of representative stations near each end of our profile where S/N s for both Ps and $SsPmp$ are large. The two sets show significant differences in both T_{Ps-Pp} and $T_{SsPmp-Ss}$. Such differences results in well-separated trade-off curves among the three unknowns (Fig. B2), indicating that the average crustal properties are distinct between the Lhasa and the Qiangtang terranes, a result consistent with previous work from the Yadong-Golmud profile along the approximately 92° E meridian (Owens and Zandt, 1997; Zhu, 1998). As such, we adopt the simplest 2D reference model for migration, with a 1D model for each of the two terranes and a smooth, linear transition in-between (Table B1).

Graphically, the procedure used to determine the value of each parameter for a particular station is as follows: Given an observed value of $T_{SsPmp-Ss}$, the trade-off between V_P and H is represented by a curve in Figure B2a. For any given pair of V_P and H , only one specific value of V_S will also satisfy observed timing of T_{Ps-Pp} at the same station (Fig. B2b). Equivalently, a known value for V_S leads to unique values for both V_P and H —two unknowns determined by two independent measurements, $T_{SsPmp-Ss}$ and T_{Ps-Pp} . For the Qiangtang terrane, we use V_S of 3.50 km/sec, the value from the isotropic model reported in Shapiro *et al.* (2004) based on dispersion of surface waves for regions near station H1620.

The corresponding value of V_S for the Lhasa terrane is about 3.55 km/sec. Two steps are involved in adopting this

value. First, a comparison of Rayleigh-wave dispersion curves within the Lhasa terrane shows comparable characteristics between the western and the central portion of this terrane (Mejia, 2001; Rapine *et al.*, 2003), indicating that there is no significant east–west variation in average crustal properties. Second, for a few stations in central Tibet, average V_S has been studied in some detail through combined inversion of Ps waveforms and Rayleigh-wave dispersion (Mejia, 2001), and we use the value of V_S reported for station SANG situated in the middle of the central Lhasa terrane.

Using combined constraints from $Ps-Pp$ and $SsPmp-Ss$, varying V_S by +0.05 km/sec in the reference model shifts K by about –0.01 (Fig. B2b). Such an effect will increase H by only about 1.5 km in the migration. In the worst case, by ignoring constraints from $SsPmp$, the change in H will approximately double, if the trade-off between K and H is based on the timing of $Ps-Pp$ alone (Zhu and Kanamori, 2000). By including the error in relative timing of ± 0.2 sec, we estimate the overall uncertainty in H to be about ± 3 km.

Table B1 lists the simplest category of models, with a linear transition between the two terranes. Using wide-angle reflections from explosions, Zhao *et al.* (2001) proposed a ramplike boundary in the midcrust across the BNS. In our case, the location of the ramp along the Moho is chosen to coincide with locations where clear Ps phase stops correlating easily with neighboring observations in unmigrated seismic profiles that are constructed from earthquakes either to the SE or to the NE of the Hi-CLIMB array. It should be noted that except for subtle shifts in crustal thickness, the exact nature and location of the transition are unimportant for the final, migrated images, as salient features of our results remain robust even if we used a single 1D reference model throughout both terranes.

Department of Earth and Atmospheric Sciences
Purdue University
West Lafayette, Indiana 47907
(R.L.N.)

Department of Geology
University of Illinois-Urbana
Urbana, Illinois 61801
(W.-P.C., T.-L.T.)